Controllable synthesis of 2D TiH$_2$ nanoflakes with superior catalytic activity for low-temperature hydrogen cycling of NaAlH$_4$

Zhuanghe Ren [a†], Xin Zhang[a†], Zhenguo Hang[b], Jianjiang Hu[c], Yangzhong Li[d], Shiyou Zheng[e*], Mingxia Gao[a], Hongge Pan[a,f*], Yongfeng Liu[a,f*]

[a]State Key Laboratory of Silicon Materials and School of Materials Science and Engineering, Zhejiang University, Hangzhou 310027, China

[b]School of Civil & Environmental Engineering, University of Technology Sydney, 81 Broadway, Ultimo, NSW, 2007, Australia.

[c]School of Chemistry and Chemical Engineering, Yantai University, Yantai 264005, China.

[d]High Performance Computing Department, National Supercomputing Center in Shenzhen, Shenzhen, Guangdong 518055, China.

[e]School of Materials Science and Engineering, University of Shanghai for Science and Technology, Shanghai 200093, China.

[f]Institute of Science and Technology for New Energy, Xi'an Technological University, Xi'an, 710021, China.

[†]These authors contributed equally to this work.
*Corresponding author:
Email: mselyf@zju.edu.cn (Y.F.L.), syzheng@usst.edu.cn (S.Y.Z.), hgpan@zju.edu.cn (H.G.P.)

Abstract:

Nanosized titanium compounds are particularly effective in catalyzing hydrogen cycling by $NaAlH_4$. Titanium hydride (TiH_2), as a catalyst, is highly interesting since it contributes hydrogen in addition to active Ti. However, it has been challenging to fabricate nanosized TiH_2 due to the strong affinity of Ti with oxygen. Herein, TiH_2 nanoflakes with a lateral size of ~10 nm and thickness of ~1 nm are successfully synthesized through a novel facile one-pot solvothermal process. In an anhydrous THF solution, LiH reacts with $TiCl_4$ rapidly at 100 °C forming TiH_2 and LiCl. The newly formed TiH_2 nucleates and grows epitaxially on the graphene surface due to the well-matched lattice parameters, giving rise to the formation of TiH_2 nanoflakes. Both theoretical calculations and experiments reveal the generation of Cl· radicals and unsaturated C=C bonds when $TiCl_4$ reacts with THF, which promotes the formation of TiH_2. The nanoflake-like TiH_2 on graphene enables an outstanding hydrogen storage performance of $NaAlH_4$, i.e., full dehydrogenation at 80 °C and hydrogenation at 30 °C and under 100 bar H_2, with a practical hydrogen capacity of 4.9 wt%, which has been never reported before.

Keywords: 2D materials, nanoflakes, titanium hydride, complex hydrides, hydrogen storage

1. Introduction

Nanocatalysts with striking new catalytic performance, including enhanced reactivity and selectivity, have attracted ever-growing interests [1-5]. In the field of hydrogen storage, Ti-based catalysts are extensively investigated for hydrogen storage reaction of light metal hydrides [6-10], especially for sodium alanate, $NaAlH_4$, a prototypical complex hydride with favourable thermodynamics and an acceptable gravimetric storage capacity [11-14]. In 1997, Bogdanović and Schwickardi reported that a few mol% of Ti alkoxides could effectively enhance reversible hydrogen storage by $NaAlH_4$ at moderate conditions [15]. Various halides, oxides, nitrides, borides and carbides of Ti were subsequently investigated in depth [11-21], and the results reveal that Ti in high oxidation states is ultimately reduced to lower valent states and even to the zerovalent state due to the strong reducibility of $NaAlH_4$ [22-24]. More importantly, considerable experimental and theoretical studies suggested that titanium hydrides (TiH_x) likely play the catalytic roles [25-29]. With the presence of TiH_2, a remarkable improvement was achieved in the hydrogenation of NaH/Al, with the formation of $NaAlH_4$ at 130 ℃ and 82 atm H_2 [25]. The *in-situ* formation of TiH_2 was observed during mechanical milling of a 1:1 NaH/Al mixture with metallic Ti powders under H_2 atmosphere [26]. $TiH_{0.71}$ and TiH_2 were also detected during hydrogenation of the TiO_2-modified $NaAlH_4$ system at various temperatures [27]. Theoretical calculations confirm the formation of Ti-H bonds in Ti-doped $NaAlH_4$ during hydrogen cycling [28]. However, $NaAlH_4$ mixed directly with commercial TiH_2 only desorbed 3.3 wt% H within 10 h at 150 ℃, which is significantly lower than the theoretical hydrogen capacity [29]. This is likely due to the large particle sizes of commercial TiH_2 and also the oxide layers on the surface. It is therefore highly desirable to achieve the high catalytic activity of TiH_x by reducing the particle

sizes to nanoscale. However, there remains a big challenge to fabricate TiH_x of a few nanometers due to the strong affinity of Ti with oxygen, and no success has been reported so far.

Preparation of metal hydrides *via* an organometallic route is a promising way to obtain extremely small particle size [30-32]. In this work, we report a success in synthesizing epitaxial TiH_2 nanoflakes on graphene (NF-TiH$_2$@G) with a lateral size of ~10 nm and thickness of ~1 nm. NaAlH$_4$ doped with 9 wt% NF-TiH$_2$@G could fully dehydrogenate at 80 ºC and take up H$_2$ at 30 ºC and under 100 bar H$_2$, with a usable hydrogen capacity of 4.9 wt%. This represents an outstanding hydrogen storage performance never reported before and may find practical applications as on-board hydrogen storage.

2. Experimental section

2.1 Sample preparation

All reagents and solvents were purchased and used as received without further purification. NF-TiH$_2$@G was synthesized by a solvothermal process under argon using titanium chloride (TiCl$_4$, 99.9%, Aladdin), lithium hydride (LiH, 99.4%, Alfa Aesar) and graphene (97%, Aladdin) as the raw materials. Five organic solvents including cyclohexane, toluene, glycol dimethyl ether, diethyl ether and tetrahydrofuran (THF) were used as the reaction media, respectively. In a typical procedure, TiCl$_4$ (2 mmol), LiH (8 mmol) and graphene (20 mg) were sequentially added to 50 mL THF in an autoclave, heated to 100 °C and dwelled for 2 h under mechanical stirring. A black precipitate of NF-TiH$_2$@G was separated from the THF solution by filtration, washed twice with THF and finally dried at 70 °C under dynamic vacuum. The NF-TiH$_2$@G was mixed with NaAlH$_4$ by ball milling at 500

rpm for 24 h under 50 bar H_2. The ball-to-sample weight ratio was approximately 120 : 1. The composites were labelled as NaAlH$_4$-x wt% NF-TiH$_2$@G (x = 0, 1, 3, 5, 7, 9 and 11).

2.2 Characterization methods

A MiniFlex 600 X-ray diffractometer (XRD) (Rigaku, Japan) with Cu K$_\alpha$ radiation (λ = 0.15406 nm) operated at 40 kV and 15 mA was used to identify the phase structure. The XRD data were collected in the 2θ range of 10-90° with a 0.05° step increment at room temperature. The samples were sealed to prevent air and moisture exposure in a custom-designed container with a window covered by Scotch tape for X-ray transmission. Scanning electron microscope (SEM) (Hitachi S-4800), aberration-corrected scanning transmission electron microscope (STEM) (Titan G^2 80-200 Chemi STEM FEI, 200 kV), aberration-corrected TEM (Titan G^2 60-300 FEI, 300 kV) and TEM (Tecnai G^2 F20 S-TWIN FEI, 200 kV) were used to observe the morphology and structure of the samples. For SEM observation, the sample was transferred quickly to the SEM facility under Ar protection. For STEM and TEM examination, the sample was protected with a double-tilt vacuum transfer holder (Gatan 648, USA). Atomic force microscope (AFM) characterization was performed on Bruker Dimension Icon under the tapping mode, with samples prepared by dropping freshly diluted sample solutions onto silicon substrates. X-ray photoelectron spectroscopy (XPS) analyses were carried out using a Thermo Scientific ESCALAB 250Xi spectrometer with a monochromatic Al Ka X-ray source at a base pressure of 6.8×10^{-9} Torr. The Ti loadings of the samples were determined by inductively coupled plasma spectroscopy (ICP) on a PE Optima 8000 instrument. Electron paramagnetic resonance (EPR) measurement was conducted using a Bruker A300 EPR Spectrometer. The spectrum of Ti(Cl$_3$) complex was recorded at 120 K and that

of Cl· radical at room temperature with N-tert-Butyl-α-phenylnitrone (PBN) as a trapping agent (10 mg/mL).

A home-built temperature programmed desorption (TPD) system attached to a mass spectrometer (MS) was employed to characterize the temperature-dependent dehydrogenation behavior using Ar as a carrier gas with a flow rate of 20 mL min^{-1}. For each test, approximately 40 mg sample was heated up from room temperature to desired temperatures at 2 °C min^{-1}. Quantitative dehydrogenation/hydrogenation properties were measured using a Sieverts-type apparatus under isothermal and non-isothermal conditions and the sample loading was approximately 70 mg sample. The non-isothermal data were acquired by gradually heating the sample from room temperature to a preset temperature at an average rate of 2 °C min^{-1} under primary vacuum (~10^{-3} Torr) for dehydrogenation and 1 °C min^{-1} with 100 bar H$_2$ for hydrogenation. The isothermal measurements were conducted by rapidly heating the sample to a desired temperature and then dwelling during the entire test. The temperature and pressure were monitored and recorded simultaneously, and the amounts of hydrogen released/uptaken were calculated based upon the ideal gas law. TGA was carried out on a Netzsch TG 209 F3 instrument under an argon atmosphere. The heating rates were identical to the volumetric experiments for isothermal dehydrogenation.

2.3 Calculation methods

All ab initio molecular dynamics (MD) simulations were performed employing the Vienna Ab initio Simulation Package (VASP) package. All atoms were described by the projected augmented plane-wave [33]. The Perdew-Burke-Ernzerhof (PBE) exchange-correlation functional [34] and a cutoff of 400 eV were used. The simulations were performed in the NVT ensemble with a time step of 1 fs, where the

temperature was kept constant at 800 K to speed up the reaction process and shorten the simulation time scale by a Nosé-Hoover chain thermostat [35,36]. A cubic simulation cell with a side length of 17.97 Å was employed for THF and 17.46 Å for cyclohexane, respectively, and both of them contains 27 molecules (351 atoms for THF and 486 atoms for cyclohexane).

3. Results and discussion

3.1 Preparation Process of TiH$_2$ Nanoflakes.

Fig. 1 illustrates a solvothermal process for the synthesis of TiH$_2$ nanoflakes. Certain amounts of organic solvents, TiCl$_4$, LiH and graphene were added in sequence into an autoclave in a glove box and then heated at 100 ℃ under constant stirring. The resultant precipitates were filtrated, washed and dried to yield the final products. Here, to optimize the synthesis, five types of organic solvents were tested, including hydrocarbons (cyclohexane and toluene) and ethers (glycol dimethyl ether, diethyl ether, and tetrahydrofuran (THF)). A strong dependence of reaction rate on the organic solvents was observed. With cyclohexane or toluene as the reaction medium, the metathesis reaction between TiCl$_4$ and LiH proceeded only partially at 100 ℃ within 6 h, as indicated by the presence of LiCl and residual LiH in the XRD profiles (**Fig. S1**a and b). When the reaction was conducted in glycol dimethyl ether, diethyl ether or THF, the reactants were completely consumed after only 2 h at 100 ℃ as evidenced by the absence of LiH (**Fig. S1**c-e). The by-product of LiCl was undetectable in the final solid product obtained in the THF solution (**Fig. S1**e), thanks to its high solubility in THF [37]. As a result, further investigations were mainly concentrated on cyclohexane and THF to understand the reaction mechanisms.

Molecular dynamics (MD) simulations were conducted to understand the reaction

processes between TiCl$_4$ and LiH in cyclohexane and THF. **Fig. 2** shows the simulated reaction between TiCl$_4$ and LiH in THF. The simulations were conducted in three-dimensional cubic boxes with side lengths of 17.97 Å for THF and 17.46 Å for cyclohexane, both of them contain 27 molecules (351 atoms for THF and 486 atoms for cyclohexane) (**Fig. 2**a and **Fig. S2**). Here, only the molecules most relevant to the reaction are shown to increase readability. Upon introducing one TiCl$_4$ molecule, one hydrogen atom attached to C2 of THF1 is attracted by a nearby chlorine atom from TiCl$_4$ and detached (**Fig. 2**b). The detached hydrogen atom in THF then combines with another hydrogen atom from C4 of THF2 to form H$_2$ (**Fig. 2**c). One chlorine atom of TiCl$_4$ interacts with the hydrogen atom attached to C1 of THF1, leading to the formation of intermediate HCl and TiCl$_3\cdot$ radical (**Fig. 2**d). The elimination of two hydrogen atoms creates an unsaturated C1=C2 bond interacting with the TiCl$_3\cdot$ radical (**Fig. 2**e). The hydrogen atom in HCl transfers to the unsaturated C4 of THF2 producing a Cl$\cdot$ radical (**Fig. 2**f). In sharp contrast, the tetrahedral structure of TiCl$_4$ remains unchanged after putting into cyclohexane during MD simulation (**Fig. S3**).

Subsequently, into the MD simulation, four LiH molecules were added to the TiCl$_4$-THF and TiCl$_4$-cyclohexane systems, respectively. In both cases, under the influence of electrophilic chlorine (Cl$\cdot$ radical, TiCl$_3$ or TiCl$_4$), most LiH dissociate and form LiCl, in both THF (**Fig. 2**g, h) and cyclohexane (**Fig. 2**i, j). In THF, some H in LiHs are bonded to Ti(Cl$_3$) to form TiH$_2$Cl (**Fig. 2**g). The newly formed TiH$_2$Cl is stabilized by the unsaturated C2 of THF1 (**Fig. 2**h) via the Ti-C interactions. In contrast, a TiH$_3$Cl$_2$-Li$_4$Cl$_2$H complex is formed in the TiCl$_4$-cyclohexane system (**Fig. 2**i, j). Further disproportionation reaction leads to the formation of TiH$_2$, for both systems. It is easier for TiH$_2$Cl to convert to TiH$_2$ by detaching one Cl atom than for TiH$_3$Cl$_2$-Li$_4$Cl$_2$H to lose two Cl atoms. The formation of the Cl$\cdot$ radicals and the

unsaturated carbon atoms during the reaction between TiCl$_4$ and THF, is therefore conducive for the formation of TiH$_2$. This explains the faster reaction between TiCl$_4$ and LiH in THF than in cyclohexane, as observed experimentally.

The MD simulation results are supported by experimental observations. First, large amounts of bubbles and fumes were observed when TiCl$_4$ was mixed with THF in a glovebox (**Video S**1), and the transparent liquid turned yellow (**Fig. S4**a and b). These phenomena indicate a chemical reaction between TiCl$_4$ and THF. Fourier transform infrared (FTIR) spectroscopy examination detected the characteristic absorbance of C=C bonding at 1625 cm^{-1} (**Fig. 3**a), indicating the formation of dihydrofuran (2,3-DHF) [38]. The change in the color can be attributed to the formation of TiCl$_4 \cdot$2THF complexes [39], which is evidenced by the red shifting and splitting of infrared bands of asymmetric and symmetric C-O-C stretching modes at 750-1250 cm^{-1} relative to pure THF (Fig. 3a) [40]. Moreover, the gaseous species evolved were identified to be H$_2$ and THF by mass spectrometry (MS) (**Fig. 3**b). Electron paramagnetic resonance (EPR) measurements show the g values of 1.80, 1.88 and 1.96 arising from unpaired electron of TiCl$_3$ complex and a characteristic seven-line spectra corresponding to Cl$\cdot$ radical (**Fig. 3**c and d) [41,42]. All these observations are in good agreement with the MD simulation results.

Based upon the theoretical and experimental results, it is believed that only a portion of TiCl$_4$ react with THF producing H$_2$, Cl$\cdot$ and TiCl$_3$-2,3-DHF. Such a chemical process completes within a short period after mixing TiCl$_4$ with THF. When a mixture of TiCl$_4$ and THF was heated to 100 ºC without dwelling, the color of the solution turned violet, indicating the formation of TiCl$_3$ complex [43]. This is corroborated by EPR measurement where a dramatic increase in the concentration of TiCl$_3$ complex was observed (**Fig. S5**). In actual experiment, LiH reacts with Cl$\cdot$

radical and $TiCl_3$ (to a certain degree) when mixed at room temperature. Upon heating to 100 ℃, the conversion of $TiCl_4$ to $TiCl_3$ and Cl· radicals accelerate (**Fig. S4**b and c), which facilitate the formation of TiH_2. We therefore believe that the formation of Cl· and $TiCl_3$ is of critical importance for promoting the fast formation of TiH_x by reacting with LiH, as simulated theoretically.

3.2 Characterization and Catalytic Activity of TiH_2 Nanoflakes.

After solvothermal treatment in THF, the resultant products, including solid and liquid, were systematically characterized by XRD, FTIR, Raman and XPS analyses. FTIR examination revealed that the filtrate was mainly composed of THF (**Fig. S6**). In addition, LiCl was also identified by XRD measurement after drying the filtrate (**Fig. S7**). The solvothermal solid product is amorphous or nanocrystalline as revealed by the XRD profile (**Fig. S1**e), and it contains Ti and C as evidenced by EDS analysis (**Fig. 4**a). The content of Ti was estimated to be ~46 wt% by ICP examination. Temperature-programmed desorption (TPD)-MS analysis reveals the evolution of H_2 upon heating (**Fig. 4**b) and the weight loss was determined to be ca. 1.8 wt% as measured by TGA (**Fig. 4**c), corresponding to 1:2 of molar ratio for Ti:H, which was further evidenced by ~4.0 wt% of weight loss for the graphene-free sample prepared by an identical solvothermal process (**Fig. S8**). This indicates the formation of TiH_2. Indeed, the typical reflections of tetragonal TiH_2 (PDF No.: 25-0983) are identified although their intensities are quite weak after heating treatement at 200 ℃ for 12 h under 100 bar of H_2 pressure (**Fig. S9**). Raman characterization also confirms the presence of graphene from the D-band (1340 cm^{-1}) and G-band (1590 cm^{-1}) peaks (**Fig. 4**d). We therefore believe that the resultant solid product consists of TiH_2 and graphene, referred as $TiH_2@G$. The chemical events in the solvothermal process are summarized in **Scheme 1**.

The obtained TiH_2 powders were first introduced to $NaAlH_4$ by ball milling at a weight concentration of 9 wt% to evaluate their catalytic activity. **Fig. 5** shows the TPD curves of $NaAlH_4$ mixed with TiH_2 prepared in different solvents. The introduction of TiH_2 remarkably reduced the temperature of hydrogen desorption from $NaAlH_4$. The solvothermal products exhibited much higher catalytic activity compared with commercial TiH_2, especially for the samples obtained in THF, glycol dimethyl ether and diethyl ether. The TiH_2 synthesized in THF exhibited relatively superior catalytic activity since its addition reduced the onset dehydrogenation temperature of $NaAlH_4$ to 80 ℃, and three desorption peaks were detected at 116, 142 and 325 ℃ upon heating. Compared with pristine $NaAlH_4$, the dehydrogenation onset temperature was lowered by 100 ℃ and three dehydrogenation peaks were reduced by 138, 125 and 29 ℃, respectively. XRD results (**Fig. S10**) reveal that below 165 ℃, $NaAlH_4$ decomposes gradually to Na_3AlH_6 and Al and finally converts to NaH and Al, agreeing with the well known two-step dehydrogenation mechanism as follows.

$$3NaAlH_4 \rightarrow Na_3AlH_6 + 2Al + 3H_2 \qquad (1)$$

$$Na_3AlH_6 \rightarrow 3NaH + Al + \frac{3}{2}H_2 \qquad (2)$$
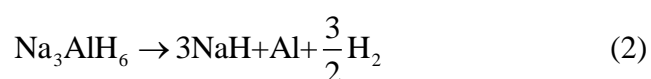
To understand the superior catalytic activity of TiH_2 prepared in THF, the morphology and microstructure were characterized along with the commercial TiH_2 by SEM, TEM, SAED and AFM. The commercial sample displays very irregular shape with a wide particle size distribution from a few to 20 μm (**Fig. S**11), while the synthesized TiH_2 adopts thin nanoflakes with a lateral size of ~10 nm dispersed on graphene (**Fig. 6**a), and 1 nm in thickness as measured by AFM (**Fig. 6**b). The SAED pattern shows a series of diffraction rings in addition to the characteristic hexagonal diffraction pattern of graphene (**Fig. 6**c and **Fig. S12**). The diffraction rings could be indexed to the (002) and (200) planes of tetragonal TiH_2. These results indicate that,

with THF as the reaction media, TiH_2 nanoflakes anchored on graphene were obtained within 2 h by a solvothermal reaction between $TiCl_4$ and LiH at 100 °C. Here, the largely reduced particle size is reasonably responsible for the remarkably lowered dehydrogenation temperature compared with the commercial TiH_2 (**Fig. S13**) and the TiH_2 prepared from Ti foils and sponge as reported recently [44]. Prolonged time or elevated temperatures caused dramatic growth of TiH_2 nanoflakes. As shown in **Fig. 6**d-f, the TiH_2 nanoflakes grew up to 50-100 nm in lateral size and ~8 nm in thickness after 4 h of solvothermal reaction at 100 °C. When the solvothermal reaction conducted at 200 °C for 2 h, the resultant TiH_2 nanoflakes are 50-200 nm in lateral size and ~20 nm in thickness, with a relatively good crystallinity (**Fig. 6**g-i). More specifically, the TiH_2 nanoflakes lay flat on the graphene, representing an out-of-plane growth. The larger TiH_2 nanoflakes show slightly reduced catalytic activity as the desorption peaks of TPD curves shift towards higher temperatures (**Fig. S**14), indicating the importance of particle sizes for catalytic activity. The smaller TiH_2 nanoflakes are apparently catalytically more active for hydrogen desorption of $NaAlH_4$, likely due to the larger number of active sites on a mass basis, and better interfacial contact between TiH_2 and $NaAlH_4$. The follow-up tests were focused on the TiH_2 nanoflakes prepared in THF within 2 h at 100 °C, which was denoted as NF-TiH_2@G hereinafter.

Further aberration-corrected TEM observation was performed to understand the growth mechanism of TiH_2 nanoflakes on graphene. As shown in **Fig. 7**a, the thickness contrast in the TEM image reveals the growth of TiH_2 nanoflakes on graphene. Fast Fourier transform (FFT) pattern (the inset of **Fig. 7**a) presents the characteristic diffraction spots assignable to (100) planes of graphene. Two pairs of diffraction spots highlighted by arrows are slightly brighter and bigger than the other

12

one, possibly due to the contribution of TiH_2 nanoflakes. HRTEM image shows that the lattice fringes of TiH_2 nanoflakes overlap closely with those of graphene (**Fig. 7**b), indicating the epitaxial growth of TiH_2 nanoflakes on graphene. The integrated pixel intensities delivered about 2.12 Å of average lattice spacings (**Fig. 7**c), agreeing well with those of (002) planes of TiH_2 (2.10 Å) and (100) planes of graphene (2.13 Å). This explains reasonably the discrepancy in the diffraction spots in FFT pattern. The lattice mismatch between the (002) planes of TiH_2 and the (100) planes of graphene was calculated to be merely 1.4%, which largely facilitates a two-dimensional growth of TiH_2 crystals on graphene [45], consequently giving rise to the formation of TiH_2 nanoflakes. The epitaxial growth of TiH_2 on graphene was schematically illustrated in **Fig. 7**d. In sharp contrast, the same synthesis process produced submicron-sized coarse particles in the absence of graphene, as shown in **Fig. S**15. This indicates unambiguously the important role played by graphene as a template for guiding the growth of nanoscaled TiH_2.

3.3 Hydrogen Storage Properties of NF-TiH₂@G-containing NaAlH₄.

To obtain the optimal amount of NF-TiH_2@G as the catalyst, seven samples with compositions of NaAlH₄-x wt% NF-TiH_2@G (x = 0, 1, 3, 5, 7, 9 and 11) were prepared by ball milling under 50 bar H_2 at 500 rpm for 24 h. **Fig. 8**a shows the hydrogen volumetric release curves with temperatures. A remarkable low-temperature shift was observed for hydrogen desorption from NaAlH₄ in the presence of NF-TiH_2@G. The addition of 1 wt% NF-TiH_2@G reduced the onset dehydrogenation temperature from 195 to 110 ℃. The first two steps of dehydrogenation completed at 205 ℃, which is 135 ℃ lower than that of pristine NaAlH₄. Increasing NF-TiH_2@G to 9 wt% induced a continuous reduction in the dehydrogenation temperatures. The NaAlH₄-9 wt% NF-TiH_2@G sample started releasing hydrogen at 80 ℃ and the

usable hydrogen capacity was measured to be 4.9 wt% while heating to 168 ℃. Such dehydrogenation temperatures are also significantly lower than those of the commercial TiH_2-modified $NaAlH_4$ (**Fig. S16**), possibly due to the uniform dispersion of NF-TiH_2@G and the good interficial contact with $NaAlH_4$ matrix cuased by largely reduced particle sizes (**Fig. S17**). For the sample with 11 wt% NF-TiH_2@G, no further reduction was obtained in the dehydrogenation temperature. Thus, the addition of NF-TiH_2@G was optimized to be 9 wt% in order to balance the dehydrogenation temperature and the usable hydrogen capacity in the present study.

More importantly, a further decrease in the dehydrogenation temperature was observed after one dehydrogenation/hydrogenation cycle. As shown in **Fig. 8**b, the onset dehydrogenation temperature was further reduced to 75 ℃ after hydrogenation at 140 ℃. This dehydrogenation onset temperature is among the lowest of the reported $NaAlH_4$ systems (**Table S1**). This is possibly related to the change in active catalytic species due to the reaction between TiH_2 and $NaAlH_4$, as discussed latter. The additional reduction in the dehydrogenation temperature can be reasonably explained by estimating the kinetic energy barriers. As shown in **Fig. 9**a and b, the activation energies were calculated to be 84 and 80 kJ mol^{-1} for the first and second steps of dehydrogenation of the activated (ie., after 1st rehydrogenation) sample, respectively, which are 6-8% lower than those of the as-milled sample. Compared with pristine $NaAlH_4$ [46], the numbers are reduced by approximately 35%, illustrating the superior catalytic activity of TiH_2 nanoflakes.

To identify the active catalytic species, the as-milled and rehydrogenated samples were washed with THF and the resultant solid state residuals were subjected to STEM observation and EDS mapping analyses (**Fig. 9**c, d). The HAADF-STEM images display nanoparticles of <5 nm in size, containing both Ti and Al as characterized by

EDS mapping. Two representative particles for the as-milled and post-activated samples (marked with yellow circles) were examined and their compositions were determined to be $Al_{85}Ti_{15}$ and $Al_{50}Ti_{50}$, respectively. We therefore believe that this change in the chemical composition could be responsible for the further improved catalytic activity after activation, as reported previously [47,48]. More importantly, the $Al_{50}Ti_{50}$ catalytic species still preserved in the following-up cycling (**Fig. S18**). It is well known that the catalytic activity of Al-Ti species arises from its favorable electronic structure for H_2 dissociation and recombination [13]. Existing theoretical calculations reveal a high energy barrier for H_2 dissociation on pure Al surface, in strictly contrast, the presence of Ti atoms on Al surface largely facilitates the absorption of H_2 molecules [49,50]. Single Ti atom on Al surface can achieve physical absorption of H_2 molecule and two Ti atoms with suitable arrangement on Al surface enable direct chemisorption of H_2 without energy barrier. As a result, $Al_{50}Ti_{50}$, with more active Ti sites because of much higher Ti content relative to $Al_{85}Ti_{15}$, is more favorable for H_2 release from $NaAlH_4$, which accounts for the further improvement of dehydrogenation performance of $NaAlH_4$ after one cycle activation. Moreover, it should be mentioned that the presence of graphene only facilitates slightly the second step of dehydrogenation and hydrogenation reaction as shown in **Fig. S16** and **Fig. 10c**. We therefore conclude that the superior catalytic activity should mainly originate from the Ti-based species.

Fig. 10 shows the isothermal dehydrogenation/hydrogenation and cycling performance of $NF-TiH_2@G$-containing $NaAlH_4$ after activation. The isothermal volumetric release curves (**Fig. 10**a) indicate that the $NF-TiH_2@G$-containing $NaAlH_4$ rapidly released 4.9 wt% within 30 min at 140 ℃. Even at 100 ℃, hydrogen released amounted to 3.9 wt% within 100 min, and further increased to 4.9 wt% after dwelling

for 800 min. More encouragingly, full dehydrogenation was achieved within 400 min while operating in TGA mode at 80 ℃ (**Fig. 10**b), where the restricting effect of hydrogen back pressure was eliminated. Such low-temperature dehydrogenation performance has not been reported before.

The fully dehydrogenated samples were rehydrogenated under 100 atm H_2 (**Fig. 10**c). Hydrogen uptake by the NF-TiH$_2$@G-containing sample occurred at remarkably reduced temperatures, starting at 30 ℃ and becoming saturated at 100 ℃. Though hydrogen uptake was also observed for the commercial TiH$_2$-modified sample at 30 ℃, it is less than 1 wt% when heated to 100 ℃. In contrast, for the dehydrogenated pristine NaAlH$_4$ sample, the absorption of hydrogen only started sluggishly above 95 ℃ under 100 bar. Further isothermal measurements showed that at temperatures as low as 30 ℃, the dehydrogenated NF-TiH$_2$@G-containing sample absorbed 4.3 wt% hydrogen within 300 min (**Fig. 10**d), and full hydrogenation was achieved after dwelling for 1000 min (**Fig. S19**). Such low-temperature hydrogenaiton capability is also largely superior to previous reports (**Table S1**). Hydrogen uptake kinetics was largely sped up at higher temperatures, and it took only 24 min for complete hydrogenation at 100 ℃. More importantly, NF-TiH$_2$@G-containing NaAlH$_4$ delivered highly stable hydrogen cycling. With an initial capacity of 4.9 wt%, only 0.1 wt% of capacity loss was detected after 50 cycles (**Fig. 8**e), corresponding to 98% of capacity retention.

To understand the stable cycling performance, the chemical states of Ti-containing active species were examined by XPS (**Fig. 11**a). No obvious change was identified in the high-resolution Ti 2p XPS spectra after 50 cycles, maintaining the characteristic 2p$_{3/2}$-2p$_{1/2}$ spin–orbit doublet of Ti in Al-Ti phase at 453.2/458.1 eV [49]. Moreover, TEM images show that Al-Ti particles maintain ultrafine sizes of less

than 5 nm (**Fig. 11**b). EDS mapping images confirm the uniform dispersion of Ti in the cycled NF-TiH$_2$@G-containing sample (**Fig. 11**c-e). Similar phenomenon was observed in a much larger scale (**Fig. S20**). As a result, the stable active catalytic species and its good dispersion are responsible for the highly stable cyclability of the NF-TiH$_2$@G-containing NaAlH$_4$.

4. Conclusions

Graphene-supported 2D TiH$_2$ nanoflakes with a lateral size of ~10 nm and thickness of ~1 nm have been successfully synthesized through a facile solvothermal synthesis based upon the reaction between TiCl$_4$ and LiH in THF. Theoretical simulation and experiments reveal that the formation of Cl· radicals and unsaturated C=C bonds are conducive to the reaction. TiH$_2$ nanoflakes epitaxially grown on graphene exhibited superior catalytic activity for hydrogen cycling of NaAlH$_4$. In TGA mode, the 9 wt% NF-TiH$_2$@G-containing NaAlH$_4$ released 4.9 wt% H at 80 °C. Such low-temperature dehydrogenation performance has not been reported previously. Full hydrogenation at 30 °C and 100 bar H$_2$ was achieved on the dehydrogenated sample. More importantly, an outstanding reversibility in hydrogen cycling was achieved with a hydrogen capacity of 4.8 wt% after 50 cycles, thanks to the stable active catalytic species with good dispersion. This work brings NaAlH$_4$ one more step closer for practical applications.

Appendix A. Supplementary data

Supplementary data associated with this article can be found in the online version at doi:

References

[1] L. L. Huang, M. H. Liu, H. X. Lin, Y. B. Xu, J. S. Wu, V. P. Dravid, C. Wolverton, C. A. Mirkin, Shape regulation of high-index facet nanoparticles by dealloying, Science 365 (2019) 1159.

[2] B. R. Cuenya, F. Behafarid, Nanocatalysis: Size- and shape-dependent chemisorption and catalytic reactivity, Surf. Sci. Rep. 70 (2015) 135.

[3] S. Cao, F. F. Tao, Y. Tang, Y. Li, J. Yu, Size- and shape-dependent catalytic performances of oxidation and reduction reactions on nanocatalysts, Chem. Soc. Rev. 45 (2016) 4747.

[4] Z. Y. Li, J. F. Li, K. H. Jiang, S. Y. Yuan, D. K. Yu, H. Wei, Z. M. Shi, X. T. Li, H. B. Chu, PdCoNi alloy nanoparticles decorated, nitrogen-doped carbon nanotubes for highly active and durable oxygen reduction electrocatalysis, Chem. Eng. J. 411 (2021) 128527.

[5] B. R. Cuenya, Metal nanoparticle catalysts beginning to shape-up, Acc. Chem. Res. 46 (2013) 1682.

[6] R. A. Varin, L. Zbroniec, M. Polanski, J. Bystrzycki, A review of recent advances on the effects of microstructural refinement and nano-catalytic additives on the hydrogen storage properties of metal and complex hydrides, Energies 4 (2011) 1.

[7] L. Z. Ouyang, K. Chen, J. Jiang, X. S. Yang, M. Zhu, Hydrogen storage in light-metal based systems: A review, J. Alloys Compd. 829 (2020) 154597.

[8] L. Li, Y. K. Huang, C. H. An, Y. J. Wang, Lightweight hydrides nanocomposites for hydrogen storage: Challenges, progress and prospects, Sci. China Mater. 62 (2019) 1597.

[9] C. J. Webb, A review of catalyst-enhanced magnesium hydride as a hydrogen storage material, J. Phys. Chem. Solid 84 (2015) 96.

[10] K. C. Xian, B. Nie, Z. G. Li, M. X. Gao, Z. L. Li, C. X. Shang, Y. F. Liu, Z. X. Guo, H. G. Pan, TiO_2 decorated porous carbonaceous network structures offer confinement, catalysis and thermal conductivity for effective hydrogen storage of LiBH4. Chem. Eng. J. 407 (2021) 127156.

[11] N. A. Ali, M. Ismail, Modification of $NaAlH_4$ properties using catalysts for solid-state hydrogen storage: A review, Int. J. Hydrogen Energy 46 (2021) 766.

[12] Y. F. Liu, Z. H. Ren, X. Zhang, N. Jian, Y. X. Yang, M. X. Gao, H. G. Pan, Development of catalyst-enhanced sodium alanate as an advanced hydrogen-storage material for mobile applications, Energy Technol. 6 (2018) 487.

[13] T. J. Frankcombe, Proposed mechanisms for the catalytic activity of Ti in $NaAlH_4$, Chem. Rev. 112 (2012) 2164.

[14] B. Bogdanović, M. Felderhoff, A. Pommerin, F. Schüth, N. Spielkamp, Advanced hydrogen-storage materials based on Sc-, Ce-, and Pr-doped $NaAlH_4$, Adv. Mater. 18 (2006) 1198.

[15] B. Bogdanović, M. Schwickardi, Ti-doped alkali metal aluminium hydrides as potential novel reversible hydrogen storage materials, J. Alloys Compd. 253 (1997) 1.

[16] B. Bogdanović, R. A. Brand, A. Marjanovic, M. Schwickardi, J. Tolle, Metal-doped sodium aluminium hydrides as potential new hydrogen storage materials, J. Alloys Compd. 302 (2000) 36.

[17] D. L. Anton, Hydrogen desorption kinetics in transition metal modified $NaAlH_4$, J. Alloys Compd. 356-357 (2003) 400.

[18] X. Z. Xiao, X. L. Fan, K. R. Yu, S. Q. Li, C. P. Chen, Q. D. Wang, L. X. Chen, Catalytic mechanism of new TiC-doped sodium alanate for hydrogen storage, J. Phys. Chem. C 113 (2009) 20745.

[19] Y. P. Fan, Z. L. Yuan, G. D. Zou, Q. R. Zhang, B. Liu, Q. Peng, Two-dimensional Mxene/A-TiO_2 composite with unprecedented catalytic activation for sodium alanate, Catal. Today 2018, 318, 167.

[20] X. Zhang, X. L. Zhang, Z. H. Ren, J. J. Hu, M. X. Gao, H. G. Pan, Y. F. Liu, Amorphous-carbon-supported ultrasmall TiB_2 nanoparticles with high catalytic activity for reversible hydrogen storage in $NaAlH_4$, Front. Chem. 8 (2020) 419.

[21] N. Sazelee, N. S. Mustafa, M. S. Yahya, M. Ismail, Enhanced dehydrogenation performance of NaAlH4 by the addition of spherical $SrTiO_3$, Int. J. Energy Res. 45 (2021) 8648.

[22] F. Schüth, B. Bogdanović, M. Felderhoff, Light metal hydrides and complex hydrides for hydrogen storage, Chem. Commun. (2004) 2249.

[23] A. Leon, D. Schild, M. Fichtner, Chemical state of Ti in sodium alanate doped with $TiCl_3$ using X-ray photoelectron spectroscopy, J. Alloys Compd. 404 (2005) 766.

[24] S. Zhang, C. Lu, N. Takeichi, T. Kiyobayashi, N. Kuriyama, Reaction stoichiometry between $TiCl_3$ and $NaAlH_4$ in Ti-doped alanate for hydrogen storage: The fate of the titanium species, Int. J. Hydrogen Energy 36 (2011) 634.

[25] K. J. Gross, E. H. Majzoub, S. W. Spangler, The effects of titanium precursors on hydriding properties of alanates, J. Alloys Compd. 356-357 (2003) 423.

[26] X. D. Kang, P. Wang, H. M. Cheng, In situ formation of Ti hydride and its catalytic effect in doped $NaAlH_4$ prepared by milling NaH/Al with metallic Ti powder, Int. J. Hydrogen Energy 32 (2007) 2943.

[27] X. Zhang, Y. F. Liu, K. Wang, M. X. Gao, H. G. Pan, Remarkably improved hydrogen storage properties of nanocrystalline TiO_2-modified $NaAlH_4$ and evolution of Ti-containing species during dehydrogenation/hydrogenation Nano Res., 8 (2015) 533.

[28] G. K. P. Dathar, D. S. Mainardi, Kinetics of hydrogen desorption in $NaAlH_4$ and Ti-containing $NaAlH_4$, J. Phys. Chem. C 114 (2010) 8026.

[29] P. Wang, C. M. Jensen, Preparation of Ti-doped sodium aluminum hydride from mechanical milling of NaH/Al with off-the-shelf Ti powder, J. Phys. Chem. B 108 (2004) 15827.

[30]B. Becker, B. Bogdanović, [TiH$_2$·(MgCl$_2$·2THF)$_{0.2-0.3}$]-the wet chemical route to a highly reactive titanium hydride, Z. Naturforsch., B: J. Chem. Sci. 50 (1995) 476.

[31]H. Bönnemann, B. Korall, Ether-Soluble Ti^0 and Bis(η^6-arene)titanium(0) Complexes from the Reduction of TiCl$_4$ with Triethylhydroborate, Angew. Chem. Int. Ed. 31 (1992) 1490.

[32]X. Zhang, Y. F. Liu, Z. H. Ren, X. L. Zhang, J. J. Hu, Z. G. Huang, Y. H. Lu, M. X. Gao, H. G. Pan, Realizing 6.7 wt% reversible storage of hydrogen at ambient temperature with non-confined ultrafine magnesium hydrides, Energy Environ. Sci. 14 (2021) 2302.

[33]J. P. Perdew, K. Burke, M. Ernzerhof, Generalized gradient approximation made simple, Phys. Rev. Lett. 77 (1996) 3865.

[34]P. E. Blöchl, Projector augmented-wave method, Phys. Rev. B 50 (1994) 17953.

[35]S. Nosé, A molecular-dynamics method for simulations in the canonical ensemble, Mol. Phys. 52 (1984) 255.

[36]S. Nosé, A unified formulation of the constant temperature molecular-dynamics methods, J. Chem. Phys. 81 (1984) 511.

[37]H. Verheyden, P. Van Lierde, M. Szwarc, G. Litvinenko, M. Van Beylen, Dual influence of lithium chloride on the anionic propagation of polystyryllithium in ethereal solvents, J. Polym. Sci., Part A: Polym. Chem. 40 (2002) 2148.

[38]F. Mauriello, E. Garrone, M. G. Musolino, R. Pietropaolo, B. Onida, Conversion of cis-2-butene-1,4-diol to hydrofurans on Pd/SiO$_2$ and Pt/SiO$_2$ catalysts under mild conditions: A Pt-Ir study, J. Mol. Catal. A: Chem. 328 (2010) 27.

[39]C. Schöttle, D. E. Doronkin, R. Popescu, D. Gerthsen, J. D. Grunwaldt, C. Feldmann, Ti^0 nanoparticles via lithium-naphthalenide-driven reduction, Chem. Commun. 52 (2016) 6316.

[40]K. Seenivasan, A. Sommazzi, F. Bonino, S. Bordiga, E. Groppo, Spectroscopic investigation of heterogeneous Ziegler-Natta catalysts: Ti and Mg chloride tetrahydrofuranates, their interaction compound, and the role of the activator, Chemistry 17 (2011) 8648.

[41] E. Morra, S. Maurelli, M. Chiesa, S. Van Doorslaer, Probing the coordination environment of Ti^{3+} ions coordinated to nitrogen-containing lewis bases, Phys. Chem. Chem. Phys. 17 (2015) 20853.

[42] Y. Zhang, J. Li, J. Bai, Z. Shen, L. Li, L. Xia, S. Chen, B. Zhou, Exhaustive conversion of inorganic nitrogen to nitrogen gas based on a photoelectro-chlorine cycle reaction and a highly selective nitrogen gas generation cathode, Environ. Sci. Technol. 52 (2018) 1413.

[43] G. Horrer, M. J. Krahfuß, K. Lubitz, I. Krummenacher, H. Braunschweig, U. Radius, N-heterocyclic carbene and cyclic (alkyl)(amino) carbene complexes of titanium(IV) and titanium(III), Eur. J. Inorg. Chem. 2020 (2020) 281.

[44] S. Suwarno, J. P. Maehlen, R. V. Denys, V. A. Yartys, Effect of oxygen on the mechanism of phase-structural transformations in O-containing titanium hydride, Int. J. Hydrogen Energy 44 (2019) 24821.

[45] C. L. Tan, J. Z. Chen, X. J. Wu, H. Zhang, Epitaxial growth of hybrid nanostructures, Nat. Rev. Mater. 3 (2018) 17089.

[46] X. Zhang, R. Y. Wu, Z. Y. Wang, M. X. Gao, H. G. Pan, Y. F. Liu, Preparation and catalytic activity of a novel nanocrystalline $ZrO_2@C$ composite for hydrogen storage in $NaAlH_4$, Chem. Asian J. 11 (2016) 3541.

[47] M. P. Pitt, P. E. Vullum, M. H. Sorby, D. Blanchard, M. P. Sulic, H. Emerich, M. Paskevicius, C. E. Buckley, J. Walmsley, R. Holmestad, B. C. Hauback, The location of Ti containing phases after the completion of the $NaAlH_4+x TiCl_3$ milling process, J. Alloys Compd. 513 (2012) 597.

[48] M. P. Pitt, P. E. Vullum, M. H. Sorby, M. P. Sulic, H. Emerich, M. Paskevicius, C. E. Buckley, J. C. Walmsley, R. Holmestad, B. C. Hauback, Functionality of the nanoscopic crystalline Al/amorphous $Al_{50}Ti_{50}$ surface embedded composite observed in the $NaAlH_4+x TiCl_3$ system after milling, J. Alloys Compd. 514 (2012) 163.

[49] A. J. Du, S. C. Smith, G. Q. Lu, The catalytic role of an isolated-Ti atom in the hydrogenation of Ti-doped Al(001) surface: An ab initio density functional theory calculation, Chem. Phys. Lett. 450 (2007) 80.

[50] S. Chaudhuri, J. Graetz, A. Ignatov, J. J. Reilly, J. T. Muckerman, Understanding the role of Ti in reversible hydrogen storage as sodium alanate: A combined experimental and density functional theoretical approach, J. Am. Chem. Soc. 128 (2006) 11404.

[51]D. E. Mencer, T. R. Hess, T. Mebrahtu, D. L. Cocke, D. G. Naugle, Surface reactivity of titanium–aluminum alloys: Ti_3Al, TiAl, and $TiAl_3$, J. Vac. Sci. Technol., A 9 (1991) 1610.
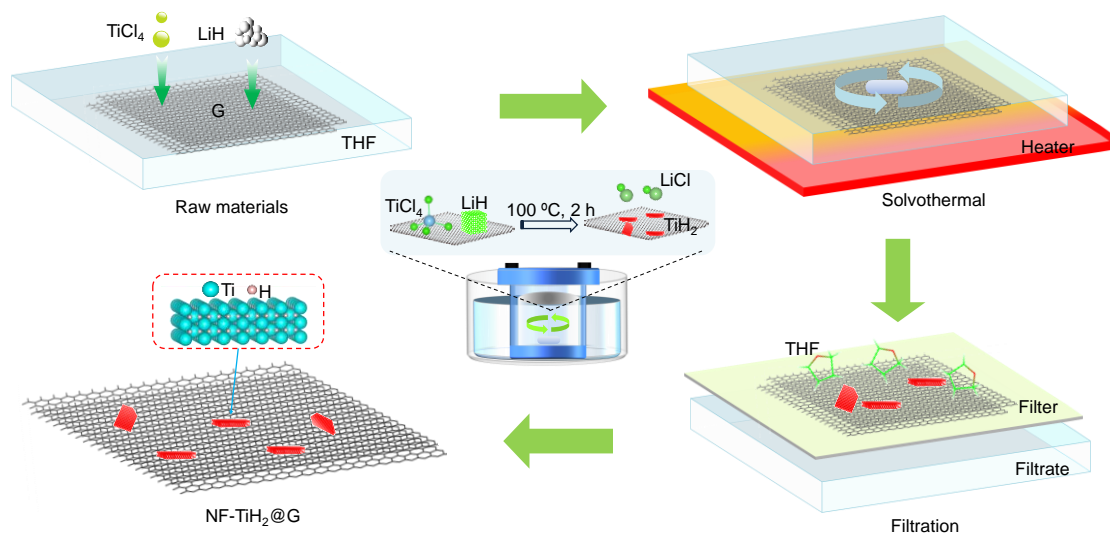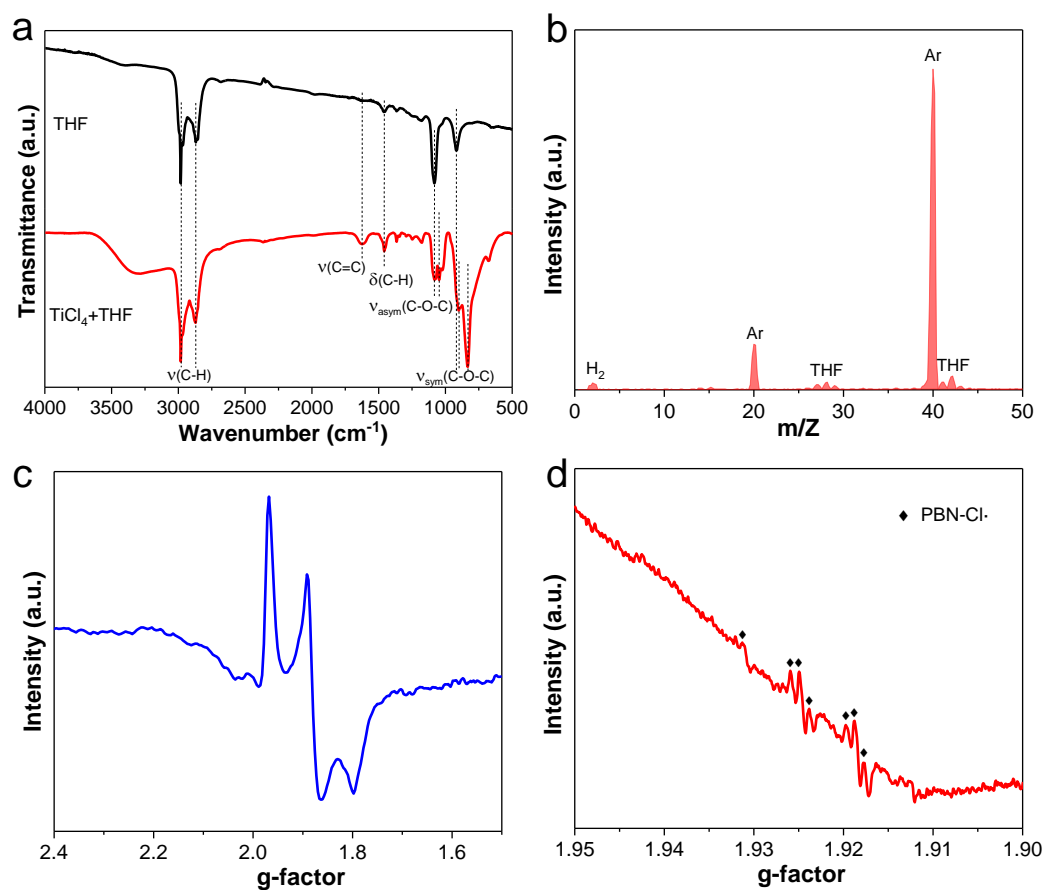
Fig. 1. Schematic illustration of the preparation of TiH$_2$ nanoflakes.
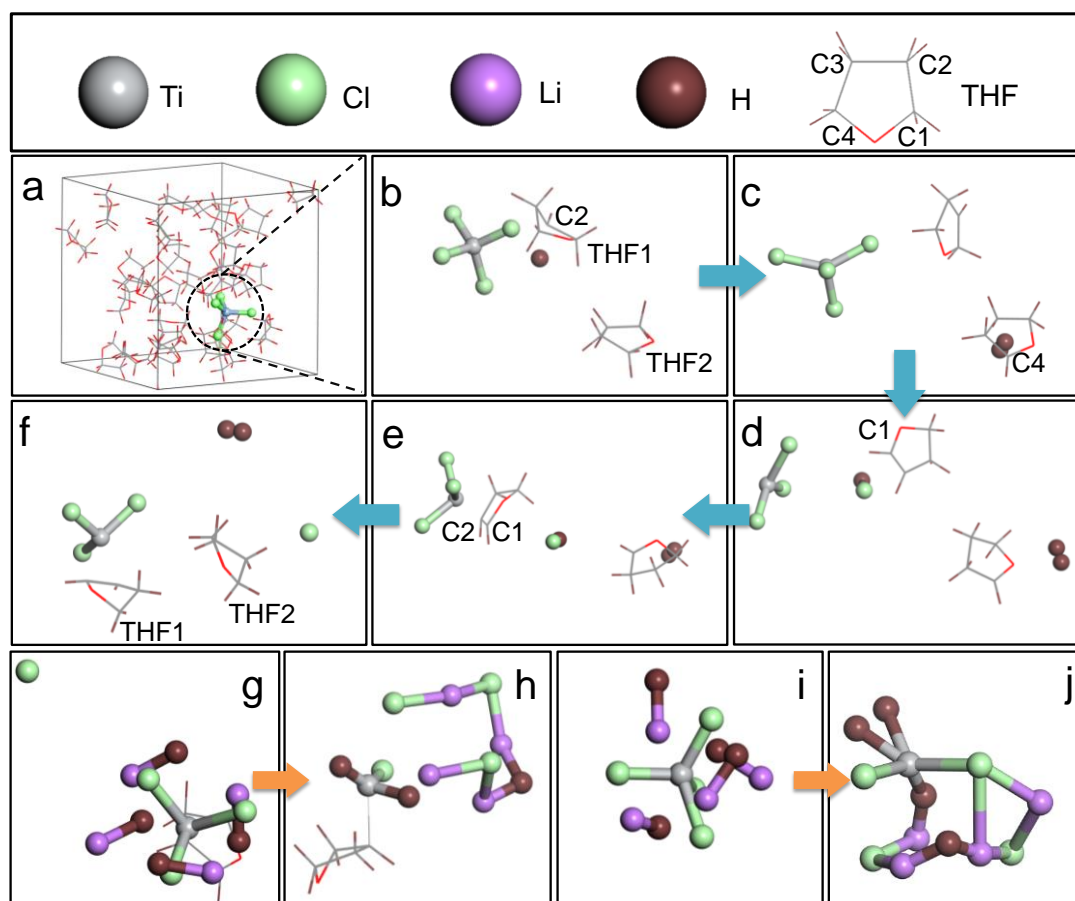
**Fig. 2.** MD simulated (a-f) reaction between TiCl$_4$ and THF, (g, i) the initial and (h, j) the final states of LiH and TiCl$_4$ after reaction in THF (g, h) and cyclohexane (i, j), respectively.

Fig. 3. (a) FTIR spectra, (b) MS signal, EPR spectra of (c) TiCl$_3$ and (d) Cl· radical with N-tert-Butyl-α-phenylnitrone (PBN) as a trapping agent (10 mg/mL) of the TiCl$_4$-THF mixture.
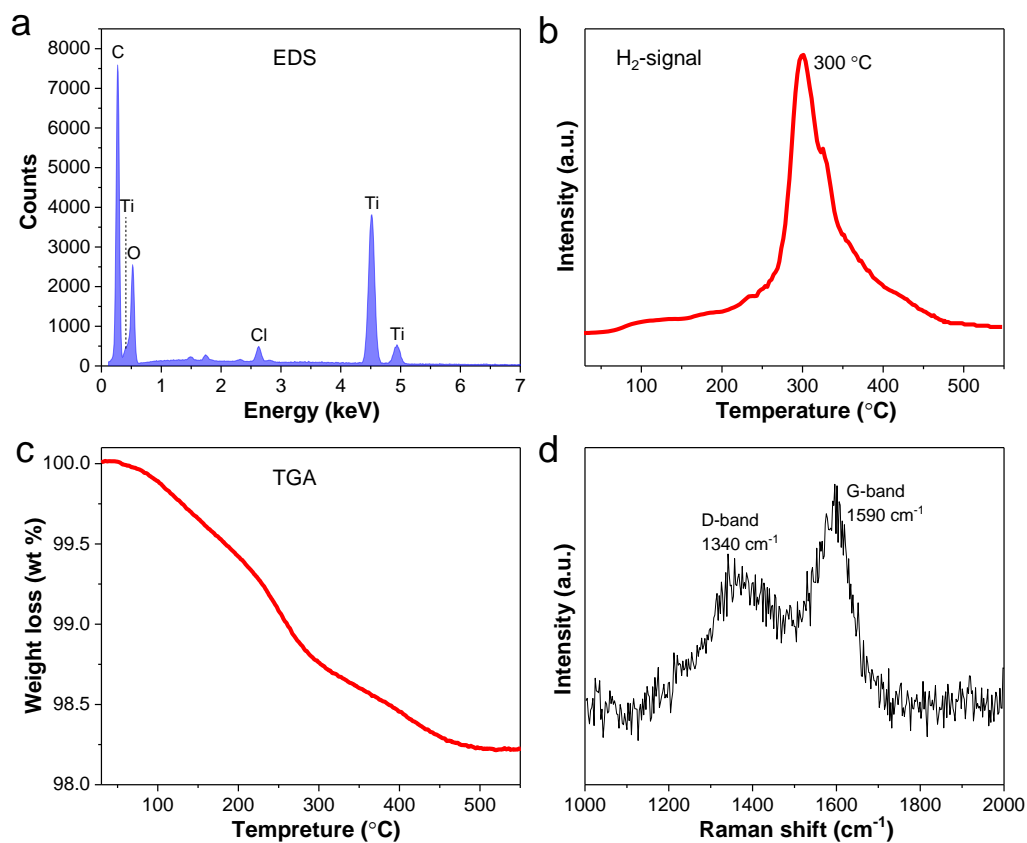
Fig. 4. (a) EDS pattern, (b) TPD-MS signal, (c) TGA curve and (d) Raman spectrum of solids obtained by reacting TiCl₄ with LiH in THF at 100 ℃ with 2 h dwell time with graphene.
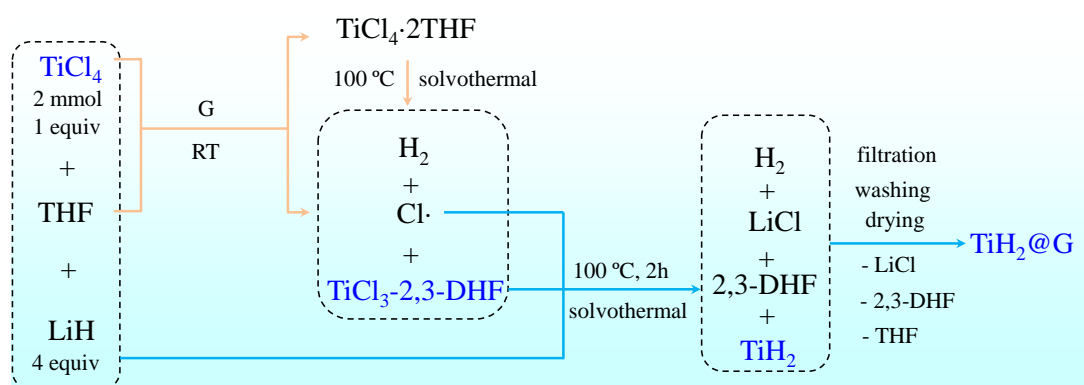
Scheme 1. Reaction process between TiCl₄ and LiH in THF.
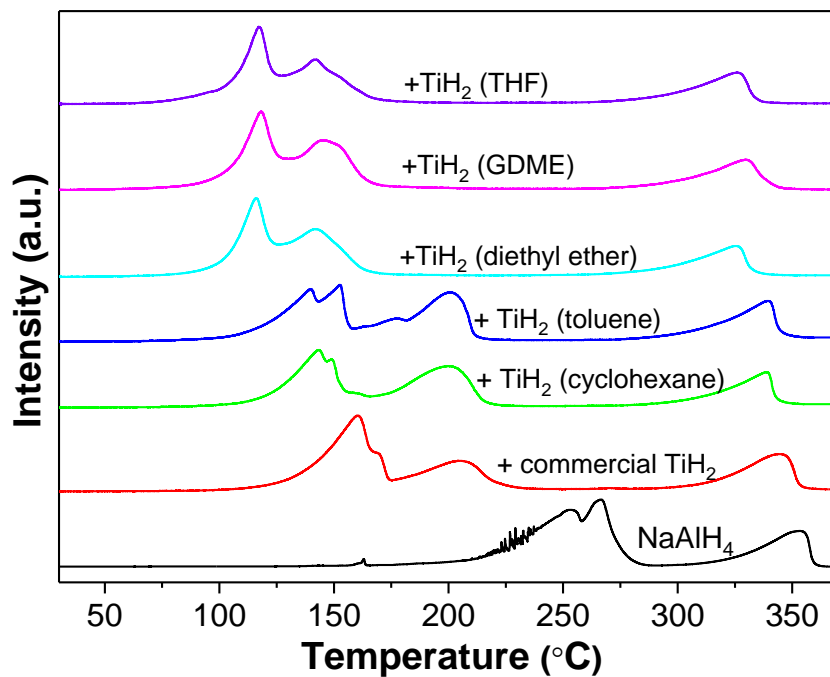
Fig. 5. TPD curves of NaAlH$_4$ doped by 9 wt% NF-TiH$_2$@G synthesized in different solvents and commercial TiH$_2$.
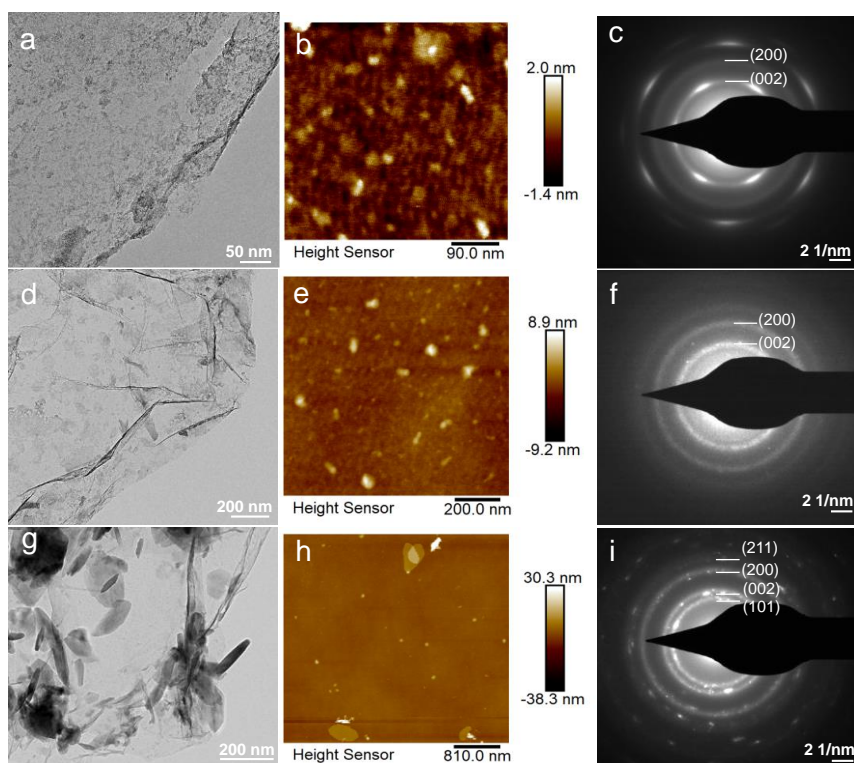

Fig. 6. TEM images, AFM images and SAED patterns of TiH$_2$ nanoflakes prepared at 100 ℃ for 2 h (a-c) and 4 h (d-f) and at 200 ℃ for 2 h (g-i).
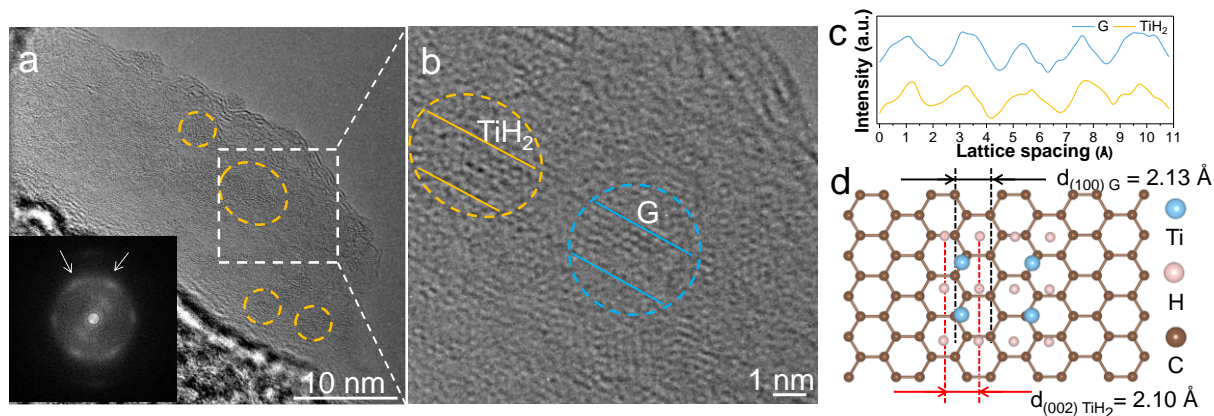
Fig. 7. (a) An aberration-corrected TEM image and (b) HRTEM image of NF-TiH$_2$@G. (c) Integrated pixel intensities of TiH$_2$ and graphene taken from the two dashed circles in (b). (d) Epitaxial growth model of TiH$_2$ nanoflakes on graphene. The inset in (a) is the corresponding FFT pattern.
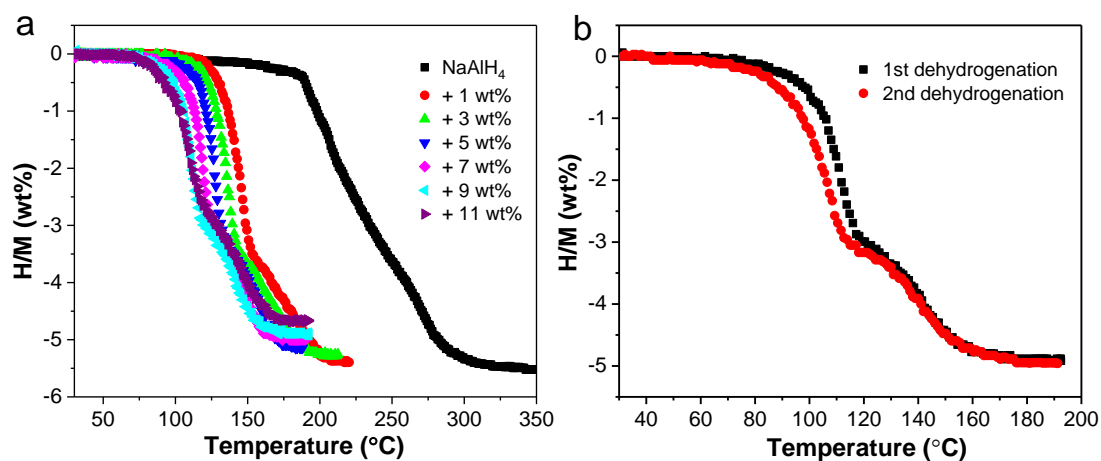

Fig. 8. (a) Volumetric hydrogen release curves of NaAlH$_4$ doped by NS-TiH$_2$@G with different weight ratio and (b) the 2nd temperature-dependent dehydrogenation curves of NaAlH$_4$-9 wt% NF-TiH$_2$@G.
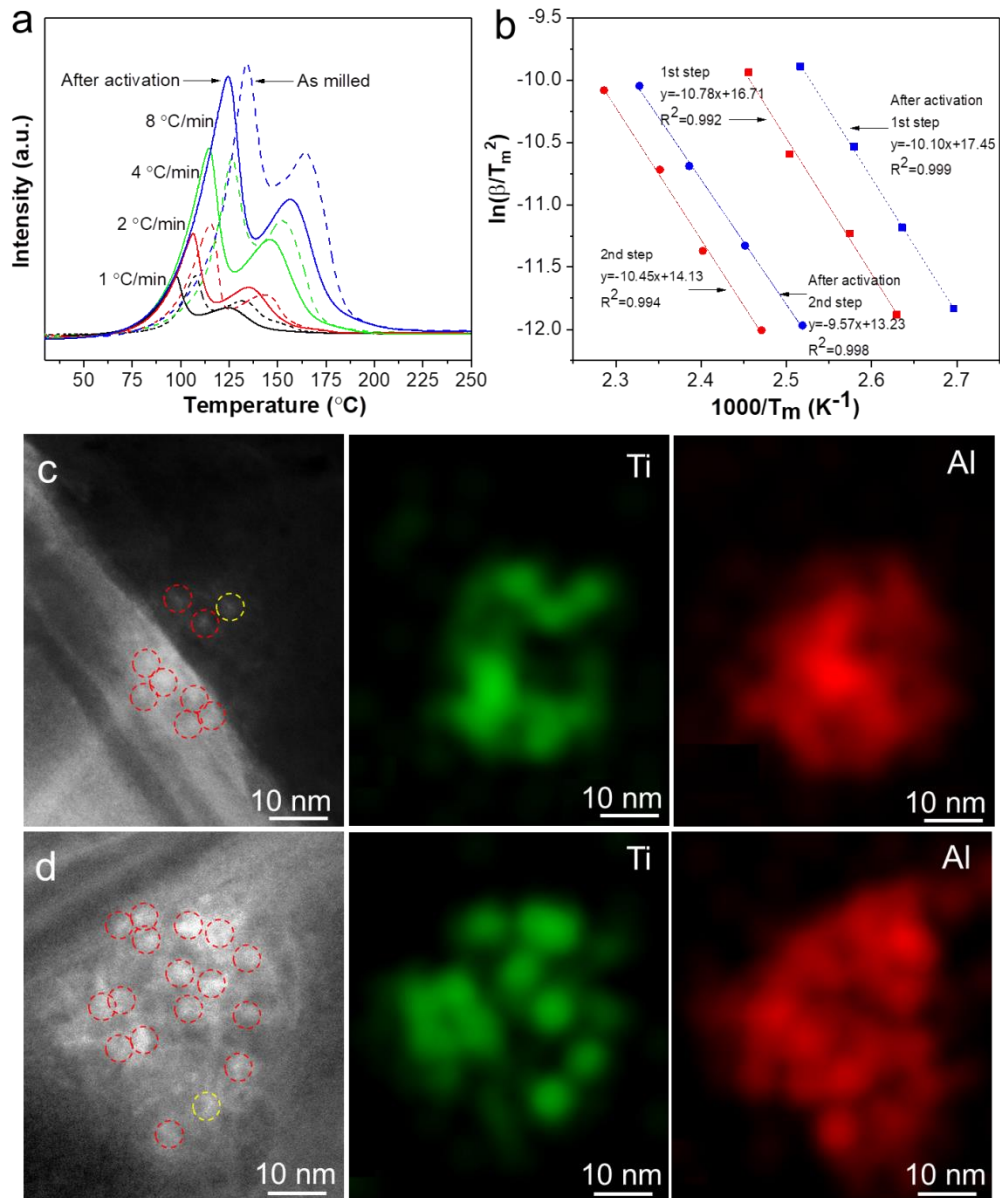
Fig. 9. (a) TPD curves, (b) Kissinger's plots and (c, d) HAADF-STEM images with Al-Ti nanoparticles highlighted by red dash circles, and the corresponding EDS mapping of NaAlH$_4$-9 wt% NF-TiH$_2$@G particles highlighted by yellow circles (c) before and (d) after the activation process.
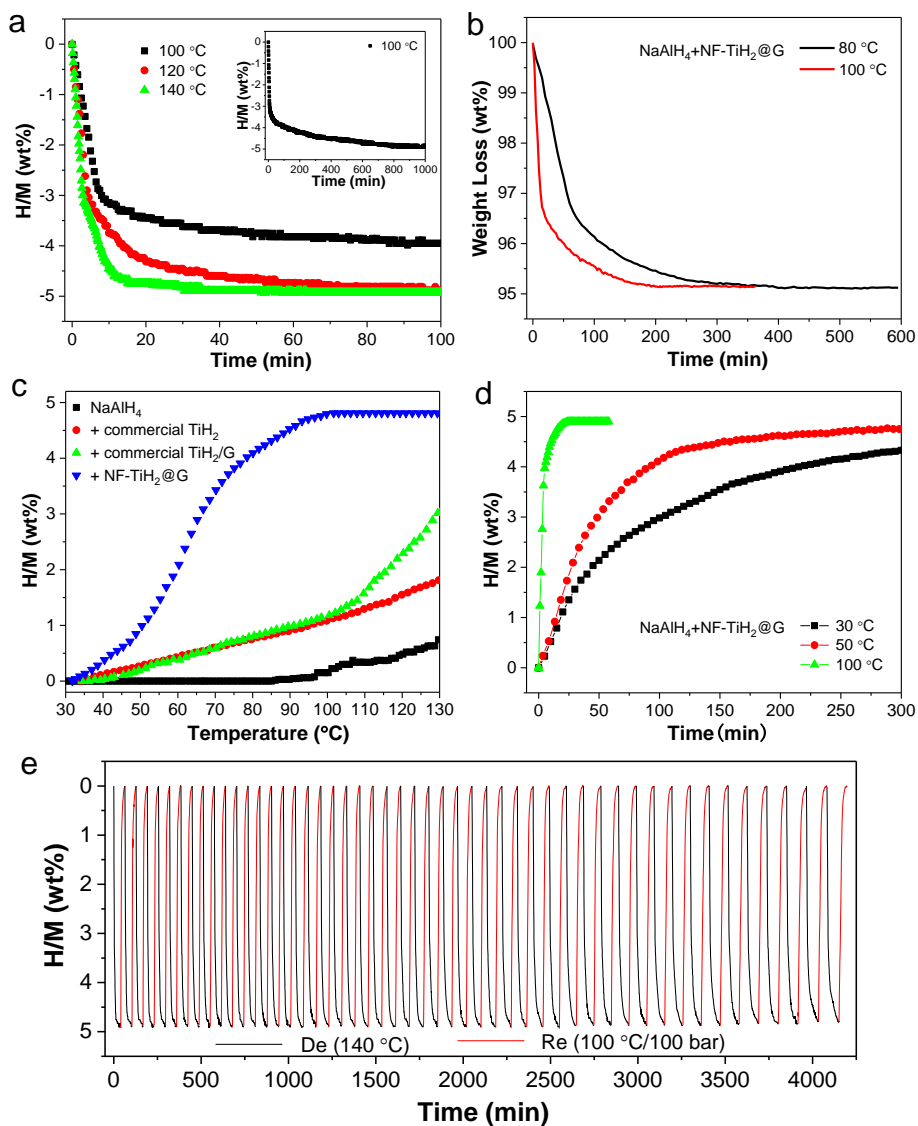
Fig. 10. (a) Isothermal dehydrogenation curves, (b) isothermal TG curves, (c) non-isothermal and (d) isothermal hydrogenation curves, and (e) cycling curves operated at 140 ℃ for dehydrogenation and 100 ℃/100 bar H_2 for hydrogenation of NaAlH$_4$-9 wt% NF-TiH$_2$@G sample.
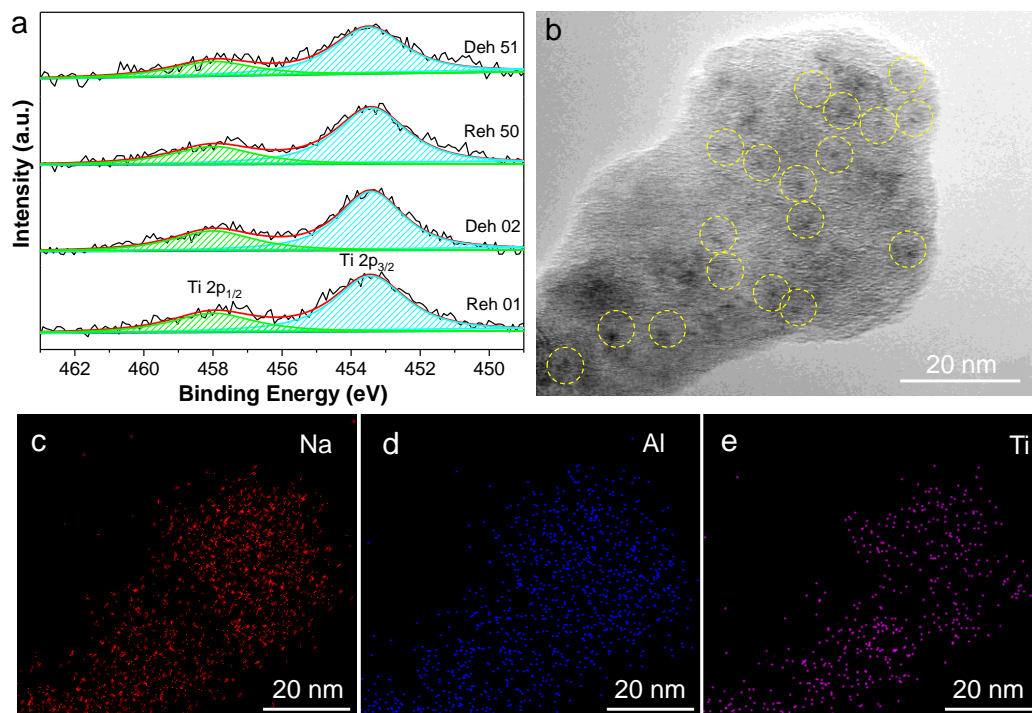
Fig. 11. (a) Ti 2p XPS spectra, (b) TEM image and (c-e) corresponding EDS

mappings of NaAlH$_4$-9 wt% NF-TiH$_2$@G sample after 50 cycles.